SCIENTIFIC REPORTS
nature research

OPEN

Probing phase transition in VO_2 with the novel observation of low-frequency collective spin excitation

Raktima Basu[1*], V. Srihari[2], Manas Sardar[3], Sachin Kumar Srivastava[3], Santanu Bera[4] & Sandip Dhara[1*]

VO_2 is well known for its first order, reversible, metal-to-insulator transition (MIT) along with a simultaneous structural phase transition (SPT) from a high-temperature metallic rutile tetragonal (R) to an insulating low-temperature monoclinic (M1) phase via two other insulating metastable phases of monoclinic M2 and triclinic T. At the same time, VO_2 gains tremendous attention because of the half-a-century-old controversy over its origin, whether electron-electron correlation or electron-phonon coupling trigger the phase transition. In this regard, $V_{1-x}Mg_xO_2$ samples were grown in stable phases of VO_2 (M1, M2, and T) by controlled doping of Mg. We have observed a new collective mode in the low-frequency Raman spectra of all three insulating M1, M2 and T phases. We identify this mode with the breather (singlet spin excitation) mode about a spin-Pierls dimerized one dimensional spin ½ Heisenberg chain. The measured frequencies of these collective modes are phenomenologically consistent with the superexchange coupling strength between V spin ½ moments in all three phases. The significant deviation of Stokes to anti-Stokes intensity ratio of this low-frequency Raman mode from the usual thermal factor exp($h\upsilon/K_BT$) for phonons, and the orthogonal dependency of the phonon and spinon vibration in the polarized Raman study confirm its origin as spin excitations. The shift in the frequency of spin-wave and simultaneous increase in the transition temperature in the absence of any structural change confirms that SPT does not prompt MIT in VO_2. On the other hand, the presence of spin-wave confirms the perturbation due to spin-Peierls dimerization leading to SPT. Thus, the observation of spin-excitations resulting from 1-D Heisenberg spin-½ chain can finally resolve the years-long debate in VO_2 and can be extended to oxide-based multiferroics, which are useful for various potential device applications.

The metal-to-insulator transition (MIT) in vanadium dioxide gains tremendous attention in scientific society because of its association with a structural phase transition (SPT). Close to room temperature (~ 340 K), VO_2 undergoes a transition from low temperature insulating to a high-temperature metallic phase along with a structural transition from monoclinic, M1 (space group $P2_1/c$) to rutile tetragonal R (space group $P4_2/mnm$)[1,2]. In addition to M1 phase, another two insulating metastable phases of monoclinic, M2 (space group $C2/m$) and triclinic, T (space group $P\bar{1}$) are also accounted to evolve in the interim of the phase transition[3,4]. The phase stabilization of the metastable phases M2 and T are reported by introducing tensile strain[5,6] along the rutile c axis (c_R) by external mechanical means or by doping with metals of lower valency than V^{4+} [7–9]. In both the insulating and metallic phases of VO_2, there exist two parallel V-chains with each vanadium atom surrounded by six oxygen forming a distorted octahedron. The schematic structures of the various phases of VO_2 are shown in Fig. 1.

The V chains are periodic and equally spaced with V-V separation of 2.86 Å in the high-temperature R phase (Fig. 1a)[10]. On the other hand, significant differences in the arrangement of V atoms along c_R axis are there in case of low-temperature monoclinic, M1, M2 and triclinic, T phases. The V atoms form pair (dimerized) alternately and tilt along the c_R axis in the M1 phase, which makes the unit cell volume double of that for the R phase with V-V separations of 2.65 (bonding) and 3.12 Å (anti-bonding) along $a_{M1} \leftrightarrow 2c_R$ axis (Fig. 1b)[7,11]. In M2 phase, one

[1]Surface and Nanoscience Division, Indira Gandhi Centre for Atomic Research, Homi Bhabha National Institute, Kalpakkam, 603102, India. [2]High pressure and Synchrotron Radiation Physics Division, Bhabha Atomic Research Centre, Mumbai, India. [3]Materials Physics Division, Indira Gandhi Centre for Atomic Research, Kalpakkam, 603102, India. [4]Water and Steam Chemistry Division, Bhabha Atomic Research Centre Facilities, Homi Bhabha National Institute, Kalpakkam, 603102, India. *email: raktimabasu14@gmail.com; dhara@igcar.gov.in

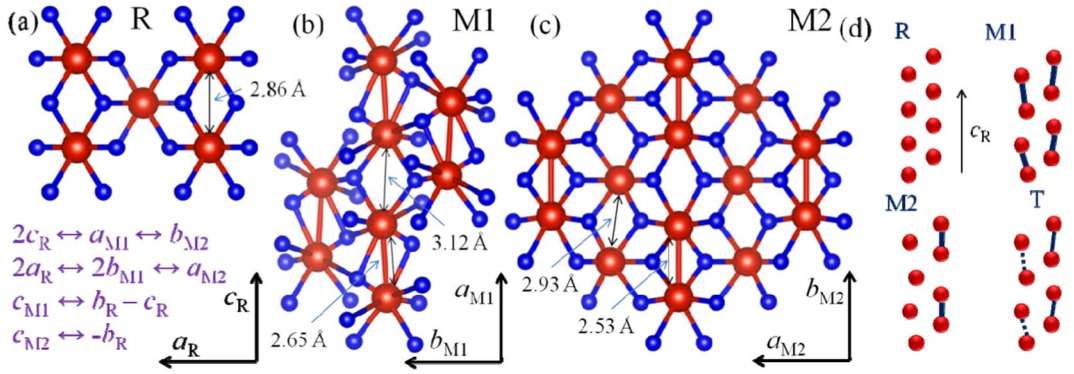

Figure 1. The schematic structures for (**a**) rutile (R), monoclinic (**b**) M1, and (**c**) M2 phases of VO_2. Red and blue balls denote vanadium and oxygen atoms, respectively. (**d**) The arrangement of vanadium chains in the four phases without oxygen atoms.

set of V chains pair along the c_R axis without being twisted and the V-V separations being 2.53 Å (bonding) and 3.25 Å (anti-bonding) along $b_{M2} \leftrightarrow 2c_R$ axis; while the V ions in the nearest neighbor V chains do not form pair but twist with respect to the c_R axis with V-V separation of 2.93 Å (Fig. 1c)[11]. The triclinic, T phase is reported as dimerized M2 phase Fig. 1d)[12]. Along with temperature, application of external electric field[13], use of hydrostatic pressure[14], radiance[15], and applied deformation[16], initiate phase transition in VO_2. Furthermore, the transition temperature (T_c) is varied by controlling the density of charge carrier[17], invoking deformation[18], or by doping[19] leading to a considerable change in the optical, electrical, and thermal properties of VO_2. These characteristics make VO_2 an attractive material, namely, windows with heat control[20], sensors for hazardous gas[21], electrical switching device[22], and cathode in Li-ion battery[23]. Doping of metal (M) in $V_{1-x}M_xO_2$ reduces[24] the T_c values for $M = Ta^{+5}$, Nb^{+5}, W^{+6}, Mo^{+6}, and increases[7–9] the T_c values for $M = Cr^{+3}$, Al^{+3}, Ga^{+3}.

As MIT is associated with SPT in this material, the debate remains, whether the electron-phonon coupling or strong electron-electron correlation trigger the phase transition[25,26]. In the present article, we study the cause of MIT and SPT and the correlation between them in details by our observation of collective spin excitation (spin-wave) for the first time in VO_2. As spin-wave propagates independently from the charge-density waves (spin-charge separation according to Tomonaga-Luttinger liquid theory), the SPT and MIT are understood by separate phenomenological model. We claim that local strain due to Mg doping leads to the transformation of the M1 phase into M2 and T phases in the $V_{1-x}Mg_xO_2$ system. Moreover, we claim that strong electron-electron correlation drives the MIT (Mott-Hubbard transition) and the V-chains in VO_2 can be considered as one-dimensional (1-D) non-interacting Heisenberg spin ½ chains. The structural phase transition is understood by the observed low-frequency Raman modes originated due to the dimerized 1-D chains resulting from Mott transition at a lower temperature. The experimentally observed Raman modes at low-frequency are compared with the calculated frequency for the singlet breather excitations in spin-Pierls dimerized state. The orthogonal dependency of the phonon and spin excitation, in the polarized Raman study helps in finding the origin of the low-frequency Raman modes as spin singlet breather excitations. Moreover, it is found that the Stokes to anti-Stokes intensity ratio of the low-frequency Raman mode differs considerably from the Boltzmann's distribution law for bosons confirming it to be originated due to collective spin excitation. The role of doping in shifting the frequency of spin-wave as well as in increasing the transition temperature while maintaining the same structural phase is discussed in details introducing finite-size 1-D Heisenberg spin ½ chain model resolving the years-long debate in the phase transition of VO_2.

Results and Discussions

The x-ray crystallographic studies of the ground free-standing samples with different Mg dopant are shown in Fig. 2a. In sample S1, the diffraction peaks confirm the presence of monoclinic M1 phase of VO_2 (JCPDS # 04-007-1466)[27]. Whereas the diffraction peaks for sample S2 match with the T phase of VO_2 (JCPDS # 01-071-0289)[28]. The samples S3 (a–d) are found out as the M2 phase of VO_2 (JCPDS # 00-033-1441)[29].

We focused on the diffraction peaks at lower 2θ values (Fig. 2b). For sample S1, the diffraction peak at $2\theta = 13.67°$ represents the (011) plane corresponding to monoclinic M1 phase (equivalent to $(110)_R$ plane) of VO_2[27]. In sample S2, two diffraction peaks observed at $2\theta = 13.47°$ and 13.81°may correspond to (−201) and (201) planes of T phase of VO_2. Similarly, for sample S3(a–d) the diffraction peaks equivalent to (−201) and (201) planes of the M2 phase of VO_2 are observed at ~ $2\theta = 13.38°$ and 13.84°. The twin peaks in samples S2 and S3(a–d) are equivalent planes of $(110)_R$ phase, which is responsible for twin crystalline formation. The T and M2 phases of $VO_2$are reported as the strained (tensile strain along the rutile c_R axis) step for the M1 phase of VO_2[6,30]. Since the samples were synthesized for different percentage of the Ar flow; there would be a different percentage of Mg dopants present in the samples. The dopant percentage can introduce strain in the sample and helps in stabilizing the T and M2 phases of VO_2. All the samples in S3 series are found out to be stabilized in M2 phase of VO_2, though the splitting of the twin peaks is observed to decrease from sample S3a ($\Delta 2\theta = 0.42°$) to S3d ($\Delta 2\theta = 0.35°$). A simultaneous decrease in the splitting of the twin peaks implies the increase in strain from sample S3a to S3d.

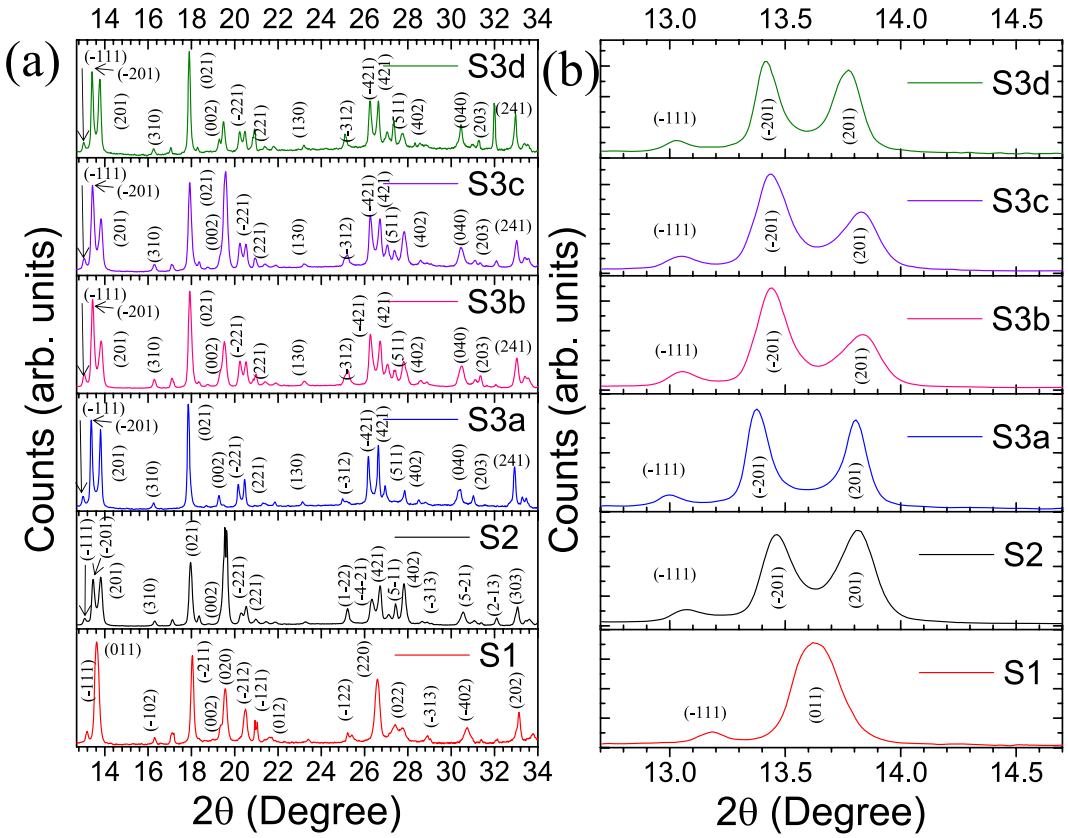

Figure 2. (**a**) The XRD pattern of the pristine samples S1, S2, and S3(a–d).The crystallographic (*hkl*) planes of the corresponding phases are indicated. (**b**) Zoomed image of the diffraction pattern for the lower angles.

In order to determine the dopant percentage in the samples, the x-ray photoelectron spectroscopy (XPS) studies were carried out for the samples S1, S2, and S3. The XPS spectra for different elements for sample S1 to S3 with the characteristic electronic transitions are shown in Fig. 3.

For sample S1, V 2*p* spin-orbit spectrum (Fig. 3a; 2nd panel) can be fitted with two curves with binding energy (BE) values of 516.3 and 523.7 eV, which are assigned as the transition from $2p_{3/2}$ and $2p_{1/2}$ spin-orbits of V^{4+}oxidization state, respectively[31,32]. No trace of Mg was observed in sample S1 (Fig. 3a; 1st and 4th panels). In case of sample S2, Mg 1s and Mg Auger peaks are observed at 1304 and 306.1 eV, respectively[33], which are reported to be observed for the Mg ion bonded with O (Fig. 3b; 1st and 4th panels). The V 2*p* spin-orbit spectrum for sample S2 can be fitted by four peaks with BE values 516.2, 518.2, 523.6, and 524.8 eV (Fig. 3b; 2nd panel). The V $2p_{1/2}$ and $2p_{3/2}$ peaks, observed at BE values of 516.2 and 523.6 eV, respectively for sample S2, can be assigned to V^{4+}oxidization state. The peaks, observed at BE value of 518.2 and 524.8 eV, can be assigned to $2p_{1/2}$ and $2p_{3/2}$ transitions for V^{5+}oxidization state[32]. In sample S3a, the peaks are identified at 516.3 and 523.7 eV for $2p_{1/2}$ and $2p_{3/2}$ transitions of V^{4+}oxidization state, respectively. Similarly, for V^{5+} oxidization state, the peaks are identified at 518.2 eV and 524.8 eV as $2p_{1/2}$ and $2p_{3/2}$ transitions in sample S3 (Fig. 3c; 2nd panel). The spin-orbit spectrum for Mg 1*s* and Mg Auger peak, in the case of sample S3a, are observed at 1304 and 306 eV, respectively (Fig. 3b; 1st and 4th panels)[33]. On the other hand, for all the samples, O1*s* peak at low BE value (530 eV) is attributed to lattice O, and O1*s* peak with high BE value (531.5 eV) corresponds to absorbed O species (Fig. 3; 3rd panel)[34,35]. The atomic percentage (at. %) of Mg, V, and O are calculated from the area under the curves considering appropriate sensitivity factors for each element and are tabulated (Table 1).

For the samples S3(b–d), we observed nearly similar results as that of sample S3a in XPS analysis except for a small increase in at. % of Mg from sample S3a to S3d (not shown in the manuscript). We have performed Laser-induced breakdown spectroscopy (LIBS) to reconfirm the identification of the trace elements present in the samples (Supplementary Fig. S1). In the case of samples S3(a–d), the intensities of Mg lines are found to increase gradually (Fig. S1). The XPS and LIBS studies confirm the presence of Mg in samples S2 and S3(a–d), which may help in stabilizing the T and M2 phase of VO_2, respectively, by introducing strain in the system (as discussed in crystallographic structural studies section). The replacement of V^{4+} (d^1) by Mg ion is more likely to produce an adjacent V^{+5} (d^0) sites in the neighboring chains. We have also carried out the x-ray absorption near edge structure (XANES) measurements to find out the oxidation state of the V in the samples (Supplementary Fig. S2). By comparing spectra, we confirm sample S1 is in +4 oxidation state, whereas samples S2 and S3 are in mixed +4 and +5 oxidation states.

The Raman spectra of the samples were collected to obtain additional information about the structural phase of the as-grown samples. The Raman spectra for of S1, S2, and S3 samples collected at 80 K are depicted in Fig. 4a.

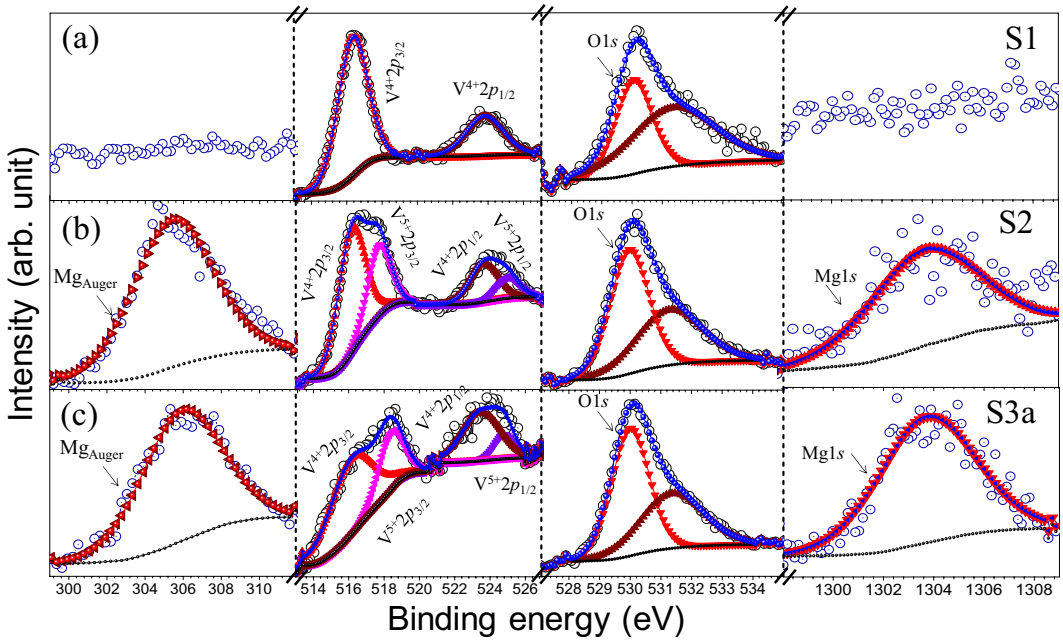

Figure 3. XPS spectra of the sample (**a**) S1, (**b**) S2, and (**c**) S3a denoted with the electronic transition of different elements. Open and solid symbols represent the data points and fitted curves, respectively.

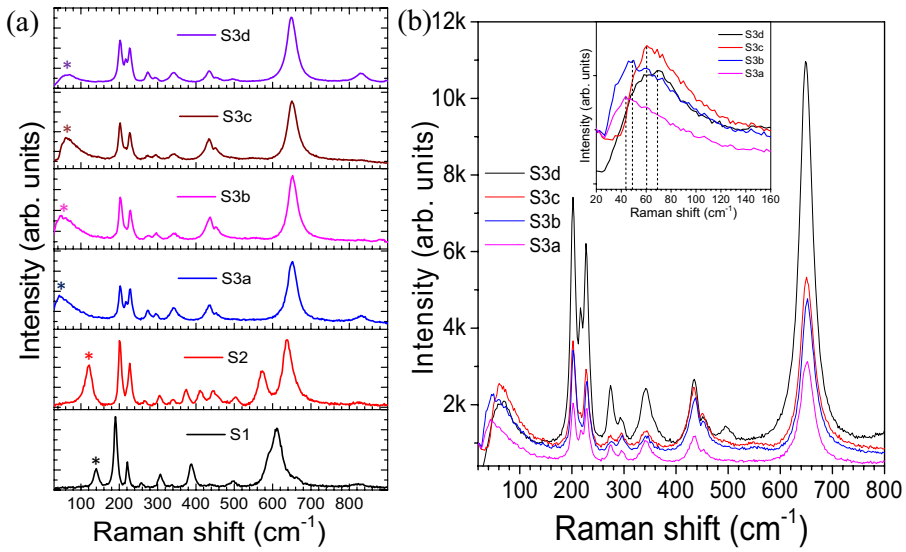

Figure 4. (**a**) Raman spectra of the samples S1 to S3 collected at 80 K and (**b**) Raman spectra for the samples S3(a–d). The inset shows a zoomed view of the Raman spectra for samples S3(a–d) at lower frequencies.

Sample	V^{4+} (at. %)	V^{5+} (at. %)	O (at. %)	Mg (at. %)	V^{5+}/V^{4+} ratio
S1	31.66	0	68.34	0	0
S2	21.42	8.19	69.57	0.81	0.38
S3a	19.77	8.50	69.75	1.97	0.43

Table 1. The atomic percentage of the elements and V^{5+}/V^{4+} ratio calculated from XPS spectra.

Eighteen Raman-active phonon modes are predicted by Group theoretical analysis for all low-temperature phases of VO_2 (for M1: $9A_g + 9B_g$, and for M2 and T: $10A_g + 8B_g$) at Γ point with different symmetries[14]. However, we observed twelve vibrational modes for sample S1 (Fig. 4a).

Observed Raman modes at 141, 190(A_g), 225(A_g), 258 (either A_g or B_g,; A_g/B_g), 307(A_g/B_g), 335(A_g), 390(A_g/B_g), 440(A_g/B_g), 497(A_g/B_g), 611(A_g), 665(B_g), 823(B_g) cm^{-1} in sample S1(Fig. 4a) conforms with pure M1 phase of

VO_2[36,37]. In sample S2, thirteen mode frequencies are observed at 121, 201(A_g), 228(A_g), 267(A_g/B_g), 304(A_g), 343(A_g), 374(A_g/B_g), 413(B_g), 445(A_g/B_g), 503(A_g/B_g), 572(A_g), 636(A_g), and 828(B_g) cm^{-1} (Fig. 4a), which match with the reported data for T phase of VO_2[4,17]. For samples S3(a–d) we observed eleven Raman modes at ~ 50, 203 (A_g), 217(A_g), 229(A_g), 273(A_g/B_g), 297(A_g), 341(A_g), 432(A_g/B_g), 454(A_g/B_g), 651(A_g), and 831(B_g) cm^{-1} (Fig. 4a), which exactly resemble with the reported M2 phase of VO_2[4,17] Raman spectroscopic studies at 80 K confirm the presence of three different phases of VO_2, i.e., M1, T, and M2 in samples S1, S2, and S3(a–d), respectively.

The Raman modes observed at 190 and 225 cm^{-1} for sample S1 are assigned to the vibration of V ions along and perpendicular to the C_R axis, respectively[4,12]. These modes are observed at 201 and 228 cm^{-1} for sample S2 and 203 and 229 cm^{-1} for sample S3. In the case of sample S3, one more Raman mode is also found to evolve at 217 cm^{-1}. The shift in frequency for the Raman mode ~190 cm^{-1} for S1 → S2 → S3 transition is 13 cm^{-1}, whereas the frequency shift for the mode ~225 cm^{-1} is only 4 cm^{-1}. The above observations imply that doping of Mg introduces strain along C_R axis and thereby stabilizing the T and M2 phase of VO_2 in samples S2 and S3(a–d), respectively. The Raman mode, observed at 611 cm^{-1} in sample S1, is due to V-O stretching vibration which shifts from 612 to 636 and 651 cm^{-1} in sample S2 and S3(a–d), respectively, indicating the length of V-O bond to be shorter with doping of Mg. In pure VO_2, V^{4+} ion is positioned at the center of the octahedron constituting of oxygen atoms, and the principal axes of the octahedron are directed perpendicular to $(110)_{M1}$ lattice plane[12]. Each V atom shared its four electrons with six neighbor O atoms, and each O atom attracted adjacent electrons supplying by three nearest V atoms. After Mg^{2+} ion occupies the native V^{4+} (+4) place, the adjacent V^{+5} (d^0) sites replace V^{4+} (d^1) sites in the neighboring chains, as observed from XPS (Fig. 3) and XANES (Fig. S2) studies. As the V^{5+} replaces V^{4+}, two apical O^{2-} of the octahedron move closer to each other resulting reduction in the V-O bond length[38]. The 141 cm^{-1} band in sample S1 is reported as A_g mode in few of the earlier reports[37,39]. However, it is also reported as an external mode in one recent article[40], which can be viewed as relative motions of structural units with respect to each other. The mode is observed at 121 cm^{-1} in sample S2 and ~50 cm^{-1} for samples S3(a–d) (denoted by "*" in Fig. 4a). The low-frequency Raman mode for samples S3(a–d) show a continuous blue-shift (inset of Fig. 4b) with an increase in doping while the other Raman peaks do not show any shift in frequency (Fig. 4b) with doping. VO_2 is reported to consist of 1-D long Heisenberg chains of V ions in two adjacent sub-lattices[12,39]. As discussed before, in the M1 phase, the V atoms dimerize forming pairs, and the pairs tilt along the c_R axis in both the sub-lattices. Whereas, in case of the M2 phase, the V chains along the c_R axis pair without twisting in one sub-lattice, while in the other sub-lattice the V chains do not form pair. Instead, they twist with respect to the c_R axis. The dimerized V chains of M2 phase slightly twist in the intermediate (between the M1 and M2 phases) T phase. The electronic structures of VO_2 were proposed by Goodenough in 1971[11]. In the electronic band structure of VO_2, the O2p orbitals form the valence band with π and σ bonds and stay 2.5 eV below the Fermi level[41,42]. In VO_2, there is single d electron per V atom and the d level splits into two states: the upper-lying doubly degenerate states e_g^{σ} states and lower-lying triply degenerate t_{2g} states. The t_{2g} states split again due to the tetragonal crystal field into an a_{1g} state (d_{xy}) and an $e_g^{\pi}\left(d_{xz},\ d_{yz}\right)$ doublet. In the low-temperature insulating phase of VO_2, V atoms dimerize along the c_R direction which makes the a_{1g} bands to be split into lower (bonding, a_{1g}) and upper (antibonding, $a_{1g'}$) bands. Moreover, the twisting of the V-V pairs away from c_R axis enhances the Vd-Op hybridization leading to a rise in the e_g^{π} band above the Fermi level. As a result, a gap of ~0.7 eV opens up and makes the insulating phase stabilized[11,12]. However, in the high-temperature metallic phase, the Fermi level crosses partially filled a_{1g} and e_g^{π} bands and the energy gap collapses. In this approach continuous changes in lattice parameters above transition temperature as well as sudden changes in lattice parameter due to V-V dimerization in the insulating phases is given as an input to calculate electronic structure, suggesting that it is the lattice that drives the MIT transition. In our previous report[39], we argued a very different scenario for MIT. In the high temperature metallic phase three bands of different orbital characters overlap. The inter-orbital Coulomb repulsion pushes up the energy levels of the upper two bands, which leads to the transfer of electrons from the upper two bands to the lowest band. The electron transfer process leads to a further level of separation between bands. This process stops when two upper bands become empty, and the lowest band becomes half filled. The changes in lattice parameters above transition temperature are driven by the changes in relative band fillings with temperature. As soon as the lower band becomes half filled, the intra-orbital local Coulomb repulsion (Hubbard-type) takes over and drives a Mott-type MIT. The Mott insulating state is nothing but an assembly of parallel spin ½ antiferromagnetic Heisenberg chain. In 1-D, Heisenberg spin chain is driven to a spin-Pierls dimerized state.

In 1D spin ½ Heisenberg system, the Hamiltonian reads as,

$$H_0 = J\sum_j S_j.\ S_{j+1} \tag{1}$$

where $J(>0)$ is the exchange interaction between neighboring spins (S). The low-energy physics of this system is usually explained by a Tomonaga-Luttinger (TL) liquid with spinon excitation[43]. The Hamiltonian H_0 and the corresponding Raman operator R_0 commute with each other, and no Raman scattering is expected without additional perturbation. However, small perturbation ν_0 exists due to spin-lattice coupling leading to the bond dimerization[44]. A perturbation due to static bond dimerizationis termed as,

$$\nu_0 = \sum_j J(-1)^j u S_j.\ S_{j+1} \tag{2}$$

where u is the distortion. Now the effective Hamiltonian becomes an exactly solvable Sine-Gordon (SG) model,

$$H' = H_0 + \int \frac{dx}{a_0} ud\ \sin(\sqrt{2\pi}\,\phi) \tag{3}$$

where $x = ja_0$; a_0 is the lattice spacing, and φ is the canonical part of Bosonic fields.

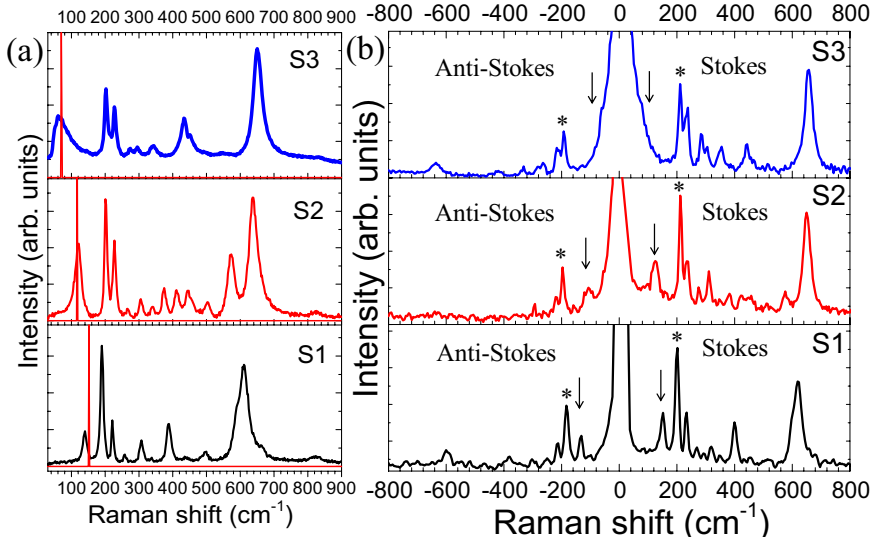

Figure 5. (**a**) Typical Raman spectra of all the samples S1 to S3a collected at 80 K and corresponding δ-functional peak at the calculated Raman mode frequency (**b**) Stokes and anti-Stokes spectra for the samples S1, S2, and S3. The spin-wave and the phonon mode used for calculation of (I_S/I_{AS}) ratio are denoted by arrow and star sign, respectively.

There are three kinds of spin excitations; soliton (S; spinon), antisoliton (S'; anti-spinon), and some breathers (B_n), which are the soliton-antisoliton (spinon-antispinon) bound states. The nth breather's mass E_n is related to E_s (mass of soliton) via $E_n = 2E_s \sin[n\pi/(8/K\text{-}2)]$

With $n = 1, \ldots, [4/K\text{-}1]$[45]. In SU(2)-symmetry, the soliton mass and second breather mass can be evaluated as

$$E_s \sim 1.5u^{2/3}J, \text{ and } E_2 = \sqrt{3}Es \tag{4}$$

Soliton, antisoliton and the first breather form a spin triplet with energy E_s. The second breather is a singlet excitation. Raman scattering from 1-D spin ½ chain is theoretically explored by Sato *et al.*[44]. It is reported that in case of dimerized chain, Raman intensity due to the triplets gives rise to a continuum background at frequencies $\omega \geq 2E_s$. Spin singlet breather B_2 appears as a δ-functional peak at $\omega = E_2$ using form-factor approach (provided $T < J$)[46,47]. However, in a practical case, a broadening in δ-functional peak is expected as the experiment is carried out at non-zero temperature.

Pouget *et al.*[48] reported the values of J for the different phases of VO_2 by the nuclear magnetic resonance (NMR) and susceptibility studies. The value of J for the M1, T, and M2 phases of VO_2 are found out as ~500 K, ~350 K, and ~320 K, respectively[48]. The distortion (u) dependence of Raman mode due to spin excitations is also reported for $CuGeO_3$, TiOCr, and others[49–51]. We have calculated the distortion ($u = \Delta l/l$, where l is the distance between two spins) for the three samples S1(M1), S2(T) and S3(M2) as $u_1 = 0.07$, $u_2 = 0.08$, and $u_3 = 0.12$, respectively. The Raman mode frequencies for the samples in M1 (S1), T (S2), and M2 (S3) phases are calculated using Eq. (4) as $\omega_1 = 152\,cm^{-1}$, $\omega_2 = 117\,cm^{-1}$, and $\omega_3 = 66\,cm^{-1}$, respectively. The calculated and experimentally observed peaks are shown in Fig. 5a.

The little variation of experimental and calculated frequency is expected as the distortion u as well as exchange interaction J depends on doping concentration and temperature. Since the breather mode frequency is proportional to $u^{2/3}J$, where u is the dimerization order parameter, its variation with temperature mimics temperature dependence of order parameter. A background luminescence is observed in the case of sample S3 (Fig. 5a), which may be due to the tilted non-dimerized and randomly dimerized V- chains as reported by Sato *et al.*[44].

To reconfirm the origin of low-frequency Raman modes, we have calculated the intensity ratio of the Stokes to anti-Stokes (I_S/I_{AS}) Raman spectra for both the spin-wave and phonon vibration as a function of temperature. The Stokes and anti-Stokes Raman spectra collected at room temperature are shown in Fig. 5b. The presence of spin-wave in both Stokes and anti-Stokes sides close to the Rayleigh line for all the three samples are denoted by an arrow mark (Fig. 5b). The frequency-shift as well as the integrated I_S/I_{AS} ratio for the spinon mode at the lowest frequency and the closest phonon mode originated due to V-V vibration ~200 cm^{-1} (denoted by '*' in Fig. 5b) are plotted as a function of temperature for all three samples (Fig. 6).

The I_S/I_{AS} ratio is compared with the Boltzmann's distribution law:

$$\frac{I_S}{I_{AS}} = \left(\frac{\upsilon - \upsilon_m}{\upsilon + \upsilon_m}\right)^4 e^{\frac{h\upsilon_m}{K_B T}} \tag{5}$$

where υ is the excitation frequency, υ_m is the phonon frequency, h is the Planck's constant, K_B is the Boltzmann's constant, and T is the temperature. The calculated values from Eq. (5) and experimentally observed values of

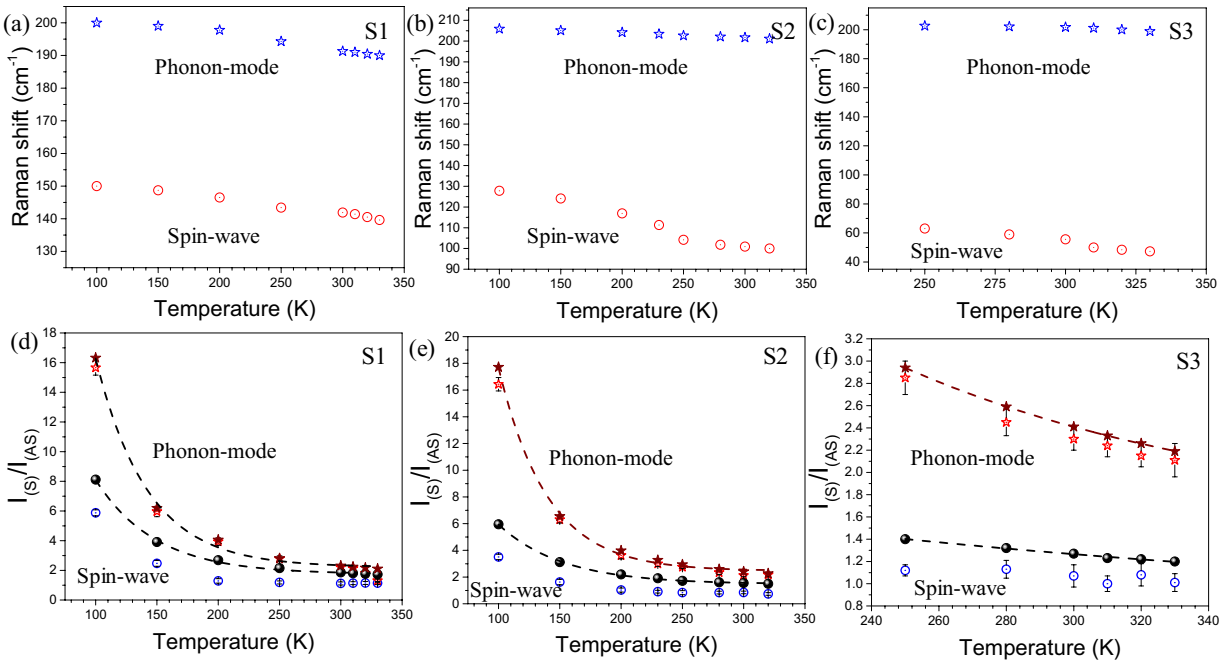

Figure 6. The frequency-shift with temperature for sample (**a**) S1, (**b**) S2, and (**c**) S3. The observed and calculated Stokes to anti-Stokes (I_S/I_{AS}) ratio with temperature for sample (**d**) S1, (**e**) S2, and (**f**) S3. The solid and empty symbols represent calculated and observed (I_S/I_{AS}) ratio, respectively, with corresponding error values.

I_S/I_{AS} ratio for both the spin-wave and the closest phonon mode are tabulated (Table 2). The calculated I_S/I_{AS} ratio are plotted in Fig. 6(d–f) as a function of temperature. It is clear from Fig. 6 that though there is a continuous red shift with an increase in temperature (Fig. 6(a–c)) for both the spin-wave and phonon mode; there is a significant mismatch between the observed I_S/I_{AS} ratio and the calculated one for the spin-wave. However, I_S/I_{AS} ratio for the closest phonon mode ~200 cm^{-1} follows the usual thermal factor of $\exp(h\upsilon/K_BT)$ following Boltzmann's distribution law.

Whereas, the lowest frequency mode for all the three samples shows a considerable deviation of I_S/I_{AS} ratio from the usual thermal factor $\exp(h\upsilon/K_BT)$ for phonons and thus confirming the mode to be originated from spin excitation[52,53]. We also performed the polarized Raman scattering on three single crystal microrods of the sample S1, S2, and S3. The FESEM image of the single microrod used for polarized Raman measurements along with randomly oriented microrods is shown in Supplementary Fig. S3a. The XRD data collected from a single microrod is also provided to confirm the orientation (Supplementary Fig. S3b). The incident excitation wave is considered along the Z direction, whereas, the growth direction of the microrods (C_R axis) is chosen along the X-axis. According to Porto notation, in the parallel $(Z(XX)\overline{Z})$ and perpendicular $(Z(YX)\overline{Z})$ polarization configurations, the first and fourth letters represent the direction of the propagation of the incident ($\boldsymbol{K}_i$) and scattered light ($\boldsymbol{K}_s$), respectively, whereas the second and third letters inside the parenthesis represents the direction of the electric field of the incident ($\boldsymbol{E}_i$) and the scattered light ($\boldsymbol{E}_s$), respectively. Figure 7 shows the Raman spectra with both parallel (XX) and cross (YX) polarization configurations for the three samples. In case of parallel (XX) polarization, the intensity of the Raman mode arising due to V-V vibration parallel to C_R axis (denoted as ω1 in Fig. 7) is more than that of the mode arising due to perpendicular to the C_R axis (denoted as ω2 in Fig. 7)[4,12,54]. Whereas, the intensity flips in case of cross (YX) polarization condition. The above observations imply the microrods are aligned along the X-axis, i.e., along the C_R direction[54]. However, the intensity of the low-frequency Raman-modes (denoted as '*' in Fig. 7) for all the three samples is observed to be high in case of cross-polarization condition ($\perp$ to C_R axis), and falls rapidly for parallel polarization ($||$ to C_R axis). As the spin chains (V-ions) are aligned along the C_R direction, the spinon vibration is expected to be produced parallel to the X-axis.

In an electromagnetic (EM) wave, the electric field vector ($\boldsymbol{E}$) and magnetic field vector ($\boldsymbol{B}$) propagates orthogonally to each other. As the excitation EM wave was incident along Z direction; while the $\boldsymbol{E}$ field propagates along the Y-axis, the $\boldsymbol{B}$ field propagates along X-axis and vice-versa. The collective spins get excited by the magnetic part of the electro-magnetic wave; therefore the maximum intensity is expected for the cross-polarization (YX) condition where $\boldsymbol{E}$ and $\boldsymbol{B}$ field propagates along the Y-axis and X-axis, respectively. Thus the orthogonal dependency of the phonon and spin excitation in the polarized Raman study reconfirms the origin of the low-frequency Raman modes as spin excitation.

We have carried out the temperature-dependent Raman spectroscopic analysis to study the phase transition of the $V_{1-x}Mg_xO_2$ samples. The temperature dependent Raman data for all the three samples S1, S2 and S3b are shown in Supplementary Fig. S4. Above the transition temperature, VO_2 became metallic in nature and we were unable to observe any Raman mode due to the screening effect. The temperature, at which sudden disappearance of all the Raman modes occurs, is considered as the transition temperature. We have also carried out temperature

T(K)	Spin-wave			Phonon mode		
	υ (cm^{-1})	$\frac{I_S}{I_{AS}}$	$\left(\frac{\upsilon-\upsilon_m}{\upsilon+\upsilon_m}\right)^4 e^{\frac{h\upsilon_m}{K_BT}}$	υ (cm^{-1})	$\frac{I_S}{I_{AS}}$	$\left(\frac{\upsilon-\upsilon_m}{\upsilon+\upsilon_m}\right)^4 e^{\frac{h\upsilon_m}{K_BT}}$
Sample S1						
100	150 ± 0.1	5.88 ± 0.2	8.12	200 ± 0.1	15.66 ± 0.5	16.32
150	148.7 ± 0.1	5.47 ± 0.2	3.91	199 ± 0.1	5.97 ± 0.35	6.2
200	146.5 ± 0.1	1.79 ± 0.15	2.69	197.8 ± 0.1	3.94 ± 0.25	4.06
250	143.4 ± 0.1	2.19 ± 0.1	2.15	194.3 ± 0.1	2.78 ± 0.2	2.81
300	141.9 ± 0.1	1.62 ± 0.1	1.86	191.3 ± 0.1	2.20 ± 0.1	2.31
310	141.4 ± 0.1	3.44 ± 0.1	1.81	191 ± 0.1	2.13 ± 0.1	2.24
320	140.5 ± 0.1	2.95 ± 0.1	1.77	190.4 ± 0.1	1.81 ± 0.1	2.17
330	139.6 ± 0.1	1.74 ± 0.1	1.73	190 ± 0.1	1.31 ± 0.1	2.11
Sample S2						
100	127.8 ± 0.1	3.41 ± 0.2	5.95	205.9 ± 0.1	16.44 ± 0.5	17.72
150	124.1 ± 0.1	2.33 ± 0.2	3.12	205.1 ± 0.1	6.30 ± 0.25	6.55
200	116.9 ± 0.1	1.93 ± 0.15	2.20	204.2 ± 0.1	3.62 ± 0.25	3.98
230	111.3 ± 0.1	3.11 ± 0.1	1.91	203.4 ± 0.1	3.00 ± 0.2	3.27
250	102.2 ± 0.1	2.54 ± 0.15	1.72	202.6 ± 0.1	2.75 ± 0.1	2.94
280	101.8 ± 0.1	1.44 ± 0.1	1.61	202.1 ± 0.1	2.35 ± 0.15	2.59
300	100.9 ± 0.1	1.25 ± 0.1	1.55	201.7 ± 0.1	2.13 ± 0.1	2.41
320	100.0 ± 0.1	1.94 ± 0.1	1.50	201.1 ± 0.1	2.17 ± 0.1	2.27
Sample S3						
250	63.0 ± 0.1	1.02 ± 0.05	1.40	202.6 ± 0.1	2.85 ± 0.15	2.94
280	58.9 ± 0.1	1.03 ± 0.08	1.32	202.1 ± 0.1	2.45 ± 0.12	2.59
300	55.6 ± 0.1	1.07 ± 0.1	1.27	201.7 ± 0.1	2.30 ± 0.1	2.41
310	50.0 ± 0.1	1.00 ± 0.07	1.23	201.1 ± 0.1	2.24 ± 0.1	2.33
320	48.4 ± 0.1	1.18 ± 0.1	1.22	200.0 ± 0.1	2.15 ± 0.1	2.26
330	47.3 ± 0.1	1.11 ± 0.08	1.20	198.9 ± 0.1	2.11 ± 0.15	2.19

Table 2. Comparison between calculated and experimentally observed I_S/I_{AS} ratio for the three samples.

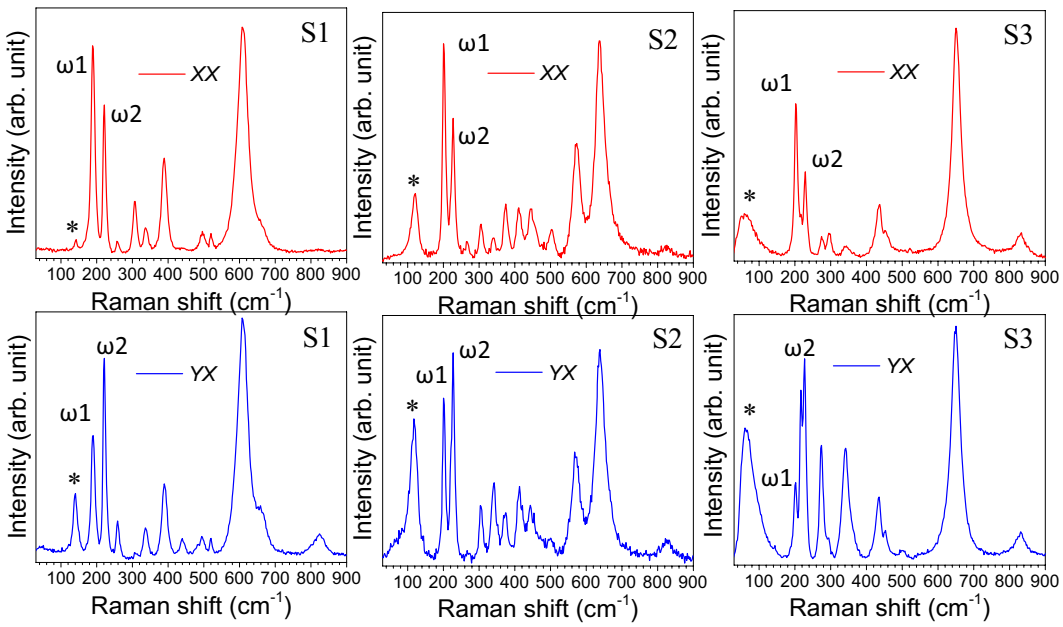

Figure 7. (**a**) Raman spectra at parallel (*XX*) and cross (*YX*) polarization condition for the three samples S1, S2, and S3.

driven resistivity measurements (Supplementary Fig. S5) to reconfirm the transition temperatures. The resistance is observed to drop ~3 to 4 orders. Figure 8a shows typical temperature-dependent Raman spectra for sample S1. All the Raman modes disappear at 340 K for S1, 345 K for S2, 348 K for S3a, 350 K for S3b, 355 K for S3c, 358 K

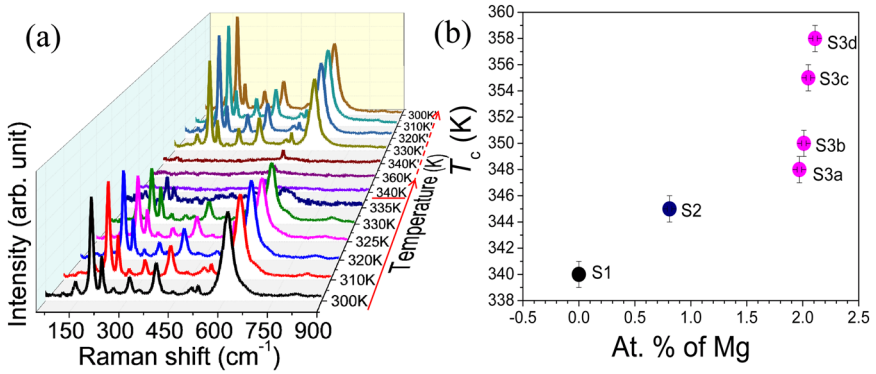

Figure 8. (**a**) Raman spectra of the sample S1 as a function of temperature. The transition temperature is underlined. Solid and dashed arrows denote the increase and decrease in temperature, respectively, and (**b**) Variation of transition temperature with at. % of Mg dopant.

for S3d confirming the transition to metallic R phase[12,39]. The transition temperature is found to increase with an increase in Mg dopant (Fig. 8b).

Doping of Mg leads to sites with V^{5+} or d^0 states (holes in the electron chains). The d^0 sites effectively cut down the length of the infinitely long 1-D spin chains into smaller fragments[39]. The average size (L) of the spin-chains decreases with increase in d^0 states, i.e., with an increase in Mg dopant. The temperature of Spin-Peierls transition in the infinite-sized system is lesser than that of in the finite-sized system. Takayoshi *et al.*[45] reported for 1D spin ½ Heisenberg chains that the finite energy gap increases linearly with $1/L$ (finite chain length ~ L). As the doping concentration of Mg increases from samples S3a to S3d, the average length of finite-sized spin ½ Heisenberg chains decreases, which in turn increases the factor $1/L$. The increase in $1/L$ results in an increase in E_s in SU(2) systems and thereby the Raman mode frequency ω increases as observed in Fig. 4b ($\omega = E_2$ and $E_2 = \sqrt{3}E_s$). The blue shift (inset of Fig. 4b) with an increase in doping is observed only for the low-frequency spinon mode, while the other vibrational modes remain unchanged (Fig. 4b) with doping. The variation in T_c with hole doping while maintaining the same monoclinic, M2 symmetry (Sample S3(a–d)) confirms that SPT does not have any role in MIT. Spin-Pierls dimerized state comes from, spin-phonon coupling in Heisenberg spin ½ antiferromagnetic chain. Heisenberg spin chain presupposes a Mott transition in a half filled band. It is to be emphasized that this spin-mode is also observed in M2 phase (insulating) where only half the V-V chains are dimerized, and the other chains are not dimerized. The fact that the un-dimerized chains are not electrically conducting suggests the metal-insulator transition is a correlation driven Mott-transition which prompts a simultaneous SPT with reduction of temperature.

Conclusions

$V_{1-x}Mg_xO_2$ samples were grown in stable phases of VO_2 (M1, M2, and T) by controlled doping of Mg. Random local strain due to Mg doping is found out as the main cause for the evolution of the M1 phase into T and M2 phases. The unrelaxed local strain in the metastable phases, however, does not bring metallicity in the system. It is argued that strong electronic correlation drives the MIT and in turn, the Mott type MIT prompts a structural transition of spin-Peierls originating at a lower temperature. The insulating phases of VO_2 can be considered as infinitely long 1-D dimerized Heisenberg spin ½ chains. The newly observed collective modes in the low-frequency Raman spectra of all three insulating M1, M2 and T phases are explained by the breather (singlet spin excitation) mode about a spin-Pierls dimerized 1-D spin ½ Heisenberg chain. The orthogonal dependency of the phonon and the singlet breathers in the polarized Raman study help in finding the origin of the low-frequency Raman modes as spin excitations. Moreover, it is found that the Stokes to anti-Stokes intensity ratio of the low-frequency Raman mode differs considerably from the Boltzmann's distribution law confirming its origin from spin excitations. The fact that the M2 phase is insulating even though half the V-V chains are not dimerized conclusively proves that MIT is a Mott-Hubbard transition. The V vacancy, invoked by Mg doping, creates d^0 sites (V^{5+}) at the nearest neighbors and introduces finite-size scaling effect by reducing the effective length of the Heisenberg spin ½ chains. Thus, the role of doping in increasing the transition temperature is understood by introducing finite-size 1-D Heisenberg spin ½ chain model. As spin-wave propagates independently from the charge-density waves, the shift in the frequency of spin-wave with doping in the absence of any structural phase transition confirms that the SPT does not prompt the MIT and resolves the years-long debate in the phase transition of VO_2.

Methods

$V_{1-x}Mg_xO_2$ microrods were grown by vapor transport process on high pure (99.99%) alumina boat using mixed VO_2 powder and Mg powder (Sigma-Aldrich, 99%) as the source and Ar (99.9%) as the carrier gas. The synthesis was carried out at 1100 K for 3 h. The concentration of the Mg dopant was controlled by changing the flow rate of the carrier gas. The synthesis was carried with the optimized flow of Ar (99.9%), e.g., 20, 40, 60, 80, and 100 sccm (samples, S2, S3a, S3b, S3c, and S3d, respectively) in the presence of Mg powder. Sample S1 was prepared with the flow of 20 sccm Ar, keeping other growth conditions same except the Mg powder. The XPS (VG ESCALAB

MK200X) analysis was performed for the elemental analysis of the VO_2 samples synthesized at different growth conditions using an x-ray source of Al-Kα (1486.6 eV) with beam diameter around 3 mm. The C 1*s* reference peak was used for calculating the BE values. A mixture of Gaussian–Lorentzian line shapes was used for fitting the spectra after applying Shirley type background correction. The structural properties of the as-grown samples were studied using synchrotron x-ray diffraction with a wavelength of 0.76089 Å using Si(111) channel cut monochromator. A MAR345 image plate area detector was used to collect the diffraction data. The vibrational modes of the synthesized samples were studied using a micro-Raman spectrometer (inVia, Renishaw, UK) in the backscattering configuration. An Ar^+ Laser (514.5 nm) was used as the excitation source along with a thermoelectrically cooled CCD camera as the detector. To carry out the polarized Raman studies, polarizer and half-wave plates were placed in the incident ray path to attain the desired configurations. The low-frequency Raman scattering measurements for the Stokes and anti-Stokes spectra were carried out using a micro-Raman spectrometer (Witec Alpha 300RA) equipped with the Bragg grating (Rayshield™). Nd-YAG laser source (532 nm) was used to excite the samples. The temperature-dependent Raman spectra were collected using a temperature-controlled stage (Linkam; THMS600) under long working distance 50X objective with a numerical aperture (N.A.) of 0.45.

Received: 9 August 2019; Accepted: 6 January 2020;
Published online: 06 February 2020

References

1. Morin, F. J. Oxides Which Show a Metal-to-Insulator Transition at the Neel Temperature. *Phys. Rev. Lett.* **3**, 34–36 (1959).
2. Haverkort, M. W. *et al*. Orbital-Assisted Metal-Insulator Transition in VO_2. *Phys. Rev. Lett.* **95**, 196404 (2005).
3. Kim, H.-T. *et al*. Monoclinic and Correlated Metal Phase in VO_2 as Evidence of the Mott Transition: Coherent Phonon Analysis. *Phys. Rev. Lett.* **97**, 266401 (2006).
4. Strelcov, E. *et al*. Doping-based stabilization of the M2 phase in free-standing VO_2 nanostructures at room temperature. *Nano lett.* **12**, 6198–6205 (2012).
5. Pouget, J. P., Launois, H., D'Haenens, J. P., Merenda, P. & Rice, T. M. Electron Localization Induced by Uniaxial Stress in Pure VO_2. *Phys. Rev. Lett.* **35**, 873–875 (1975).
6. Park, J. H. *et al*. Measurement of a solid-state triple point at the metal-insulator transition in VO_2. *Nature* **500**, 431–434 (2013).
7. Marezio, M., Dernier, P. D. & Santoro, A. Twinning in Cr-doped VO_2. *Acta Cryst. A* **29**, 618–621 (1973).
8. Villeneuve, G. *et al*. Magnetic and structural properties of stoichiometric and non-stoichiometric $(V,Al)O_2$ alloys. *J. Phys. C: Solid State Phys.* **10**, 3621 (1977).
9. Brückner, W. *et al*. Phase transitions and semiconductor-metal transition in $V_{1-x}Ga_xO_2$ Single Crystals. *phys. status solidi A* **38**, 93–102 (1976).
10. Zylbersztejn, A. & Mott, N. F.Metal-insulator transition in vanadium dioxide. *Phys. Rev. B* **11**, 4383 (1975).
11. Goodenough, J. B. The two components of the crystallographic transition in VO_2. *J. Solid State Chem.* **3**, 490–500 (1971).
12. Eyert, V. The metal-insulator transitions of VO_2: A band theoretical approach. *Ann. Phys. (Leipzig)* **11**, 650–702 (2002).
13. Kim, H.-T., Chae, B.-G., Youn, D.-H., Kim, G. & Kang, K.-Y. Raman study of electric-field-induced first-order metal-insulator transition in VO_2-based devices. *Appl. Phys. Lett.* **86**, 242101 (2005).
14. Marini, C. *et al*. Optical properties of $V_{1-x}Cr_xO_2$ compounds under high pressure. *Phys. Rev. B* **77**, 235111 (2008).
15. Cavalleri, A., Dekorsy, T., Chong, H. H. W., Kieffer, J. C. & Schoenlein, R. W. Evidence for a structurally-driven insulator-to-metal transition in VO_2: A view from the ultrafast timescale. *Phys. Rev. B* **70**, 161102 (2004).
16. Kikuzuki, T. & Lippmaa, M. Characterizing a strain-driven phase transition in VO_2. *Appl. Phys. Lett.* **96**, 132107 (2010).
17. Chen, C. *et al*. Influence of defects on structural and electrical properties of VO_2 thin films. *J. Appl. Phys.* **110**, 023707 (2011).
18. Atkin, J. M. *et al*. Strain and temperature dependence of the insulating phases of VO_2 near the metal-insulator transition. *Phys. Rev. B* **85**, 020101 (2012).
19. Lee, S. *et al*. Axially engineered metal-insulator phase transition by graded doping VO_2 nanowires. *J. Am. Chem. Soc.* **135**, 4850–4855 (2013).
20. Mlyuka, N., Niklasson, G. & Granqvist, C.-G. Mg doping of thermochromic VO_2 films enhances the optical transmittance and decreases the metal-insulator transition temperature. *Appl. Phys. lett.* **95**, 171909 (2009).
21. Prasad, A. K. *et al*. Novel single phase vanadium dioxide nanostructured films for methane sensing near room temperature. *Sens. Actuators B* **191**, 252–256 (2014).
22. Rajeswaran, B. & Umarji, A. M. Effect of W addition on the electrical switching of VO_2 thin films. *AIP Adv.* **6**, 035215 (2016).
23. Nethravathi, C. *et al*. N-doped graphene–VO_2 (B) nanosheet-built 3D flower hybrid for lithium ion battery. *ACS Appl. Mater. Interfaces* **5**, 2708–2714 (2013).
24. Fisher, B. Electrical and seebeck effect measurements in Nb doped VO_2. *J. Phys. Chem. Solids* **43**, 205–211 (1982).
25. Wentzcovitch, R. M. VO_2: Peierls or Mott-Hubbard? A view from band theory. *Phys. Rev. Lett.* **72**, 3389–3392 (1994).
26. Rice, T. M., Launois, H. & Pouget, J. P. Comment on "VO_2: Peierls or Mott-Hubbard? A view from band theory". *Phys. Rev. Lett.* **73**, 3042 (1994).
27. Goodenough, J. & Hong, H. Y. Structures and a Two-Band Model for the System $V_{1-x}Cr_xO_2$. *Phys. Rev. B* **8**, 1323 (1973).
28. Marezio, M., McWhan, D. B., Remeika, J. P. & Dernier, P. D. Structural Aspects of the Metal-Insulator Transitions in Cr-Doped VO_2. *Phys. Rev. B* **5**, 2541 (1972).
29. Mitsuishi, T. On the phase transformation of VO_2. *Jpn. J. Appl. Phys.* **6**, 1060 (1967).
30. Nazari, M. *et al*. Temperature dependence of the optical properties of VO_2 deposited on sapphire with different orientations. *Phys. Rev. B* **87**, 035142 (2013).
31. Colton, R. J., Guzman, A. M. & Rabalais, J. W. Electrochromism in some thin-film transition-metal oxides characterized by x-ray electron spectroscopy. *J. Appl. Phys.* **49**, 409–416 (1978).
32. Nag, N. & Massoth, F. ESCA and gravimetric reduction studies on V/Al_2O_3 and V/SiO_2 catalysts. *J. Catal.* **124**, 127–132 (1990).
33. Seyama, H. & Soma, M. X-ray photoelectron spectroscopic study of montmorillonite containing exchangeable divalent cations. *J. Chem. Soc. Faraday Trans. I* **80**, 237–248 (1984).
34. Montero, I., Galán, L., de la Cal, E., Albella, J. M. & Pivin, J. C. Incorporation of OH radicals in anodic silicon oxide films studied by secondary-ion mass spectroscopy, X-ray photoelectron spectroscopy and IR analysis. *Thin Solid Films* **193**, 325–332 (1990).
35. Carnera, A. *et al*. On the formation of silicon oxynitride by ion implantation in fused silica. *J. Non-cryst. Solids* **125**, 293–301 (1990).
36. Srivastava, R. & Chase, L. Raman Spectrum of Semiconducting and Metallic VO_2. *Phys. Rev. Lett.* **27**, 727 (1971).
37. Schilbe, P. Raman scattering in VO_2. *Phys. B: Condensed Matter* **316**, 600–602 (2002).
38. Chen, C. & Fan, Z. Changes in VO_2 band structure induced by charge localization and surface segregation. *Appl. Phys. Lett.* **95**, 262106 (2009).

39. Basu, R., Sardar, M., Bera, S., Magudapathy, P. & Dhara, S. The role of 1-D finite size Heisenberg chains in increasing the metal to insulator transition temperature in hole rich VO_2. *Nanoscale* **9**, 6537 (2017).
40. Wu, X. *et al*. THz Transmittance and Electrical Properties Tuning across IMT in Vanadium Dioxide Films by Al Doping. *ACS Appl. Mater. Interfaces* **8**, 11842–11850 (2016).
41. Verleur, H. W., Barker, A. S. Jr. & Berglund, C. N. Optical Properties of VO2 between 0.25 and 5 eV *Phys. Rev*. **172**, 788 (1968).
42. Powell, R. J., Berglund, C. N. & Spicer, W. E. Photoemission from VO_2. *Phys. Rev.* **178**, 1410 (1969).
43. Giamarchi, T. *Quantum Physics in One Dimension* (Oxford Univ. Press, New York, (2004).
44. Sato, M., Katsura, H. & Nagaosa, N. Theory of Raman scattering in one dimensional quantum spin-½ antiferromagnets. *Phys. Rev. Lett.* **108**, 237401 (2012).
45. Takayoshi, S. & Sato, M. Coefficients of bosonized dimer operators in spin-½ XXZ chains and their applications. *Phys. Rev. B* **82**, 214420 (2010).
46. Essler F.H. L. & Konik, R. M. Applications of massive integrable quantum field theories to problems in condensed matter physics. arXiv:*cond-mat*/0412421.
47. Kuzmenko, I. & Essler, F. H. L. Dynamical correlations of the spin-½ Heisenberg XXZ chain in a staggered field. *Phys. Rev. B* **79**, 024402 (2009).
48. Pouget, J. P. & Launois, H. Dimerization of a linear Heisenberg chain in the insulating phases of $V_{1-x}Cr_xO_2$ *Phys. Rev. B* **10**, 1801 (1974).
49. Muthukumar, V. N. *et al*. Frustration-induced Raman scattering in $CuGeO_3$. *Phys. Rev. B* **54**, R9635 (1996).
50. Van Loosdrecht, P. H. M., Zeman, J., Martinez, G., Dhalenne, G. & Revcolevschi, A. Magnetic Interactions and the Pressure Phase Diagram of $CuGeO_3$. *Phys. Rev. Lett.* **78**, 487 (1997).
51. Ruckamp, R. *et al*. Zero-Field Incommensurate Spin-Peierls Phase with Interchain Frustration in TiOCl. *Phys. Rev. Lett.* **95**, 097203 (2005).
52. Bates, P. A., Cottam, M. G. & Smith, S. R. P. "Anomalous" behavior of the anti-stokes-stokes intensity ratio for one-magnon Raman scattering in FeF_2. *Solid State Commun.* **33**, 129 (1980).
53. White, R. M., Nemanich, R. & Herring, C. Light scattering from magnetic excitations in orthoferrites. *Phys. Rev. B* **25**, 1822 (1982).
54. Basu, R. *et al. J. Phys. Chem. C* **123**, 11189 (2019).

Acknowledgements

We thank S. G. Maji of Materials Chemistry Division, IGCAR for LIBS analysis, D. Bhattacharyya, Abharana N. and N. Tiwari of Atomic and Molecular Physics Division, BARC, Mumbai for XANES analysis, and V. Sivasubramanian of Condensed Matter Physics Division, IGCAR for fruitful discussions.

Author contributions

R.B. planned the work, executed experiments, analyzed data, and wrote the manuscript. V.S. carried out the XRD experiments. S.K.S. carried out the low frequency Raman experiments. S.B. performed the XPS experiments. M.S. and S.D. contributed in careful evaluation of manuscript and understanding. All authors discussed the results, commented on the manuscript and gave approval to the final version of the manuscript.

Competing interests

The authors declare no competing interests.

Additional information

Supplementary information is available for this paper at https://doi.org/10.1038/s41598-020-58813-x.

Correspondence and requests for materials should be addressed to R.B. or S.D.

Reprints and permissions information is available at www.nature.com/reprints.

Publisher's note Springer Nature remains neutral with regard to jurisdictional claims in published maps and institutional affiliations.